Nanoscale

PAPER

View Article Online
View Journal | View Issue

Cite this: *Nanoscale*, 2026, **18**, 4146

Monolithic photonic architecture for volumetric illumination in plasmonic photocatalysis

Abraham J. Offen, [a] Wenhao Li,[a] Dmitrii Tsvetkov,[a] Jiawei Liang,[a] Yogendra K. Mishra, [b] Natalia M. Litchinitser[a] and Jie Liu *[a]

Received 17th October 2025,
Accepted 17th January 2026

DOI: 10.1039/d5nr04370k

rsc.li/nanoscale

Recent research in high-temperature photocatalysis is rapidly revealing the unique advantages of using light to augment or replace pure thermal energy in chemical synthesis. However, poor penetration of light into a typical powder catalyst creates a major challenge for efficient photo-driven processes. This article presents a novel plasmonic catalyst system with a 3D photonic design that reshapes the balance between thermal, optical, and mass transport. This unique 3D porous architecture allows for the catalyst bed to be illuminated volumetrically while improving mass transport over traditional aerogels. When compared to a powdered catalyst, this monolithic supported plasmonic Rh/SiO_2 catalyst exhibits dramatically increased response to light, both in increased reaction rate and improved selectivity for CO_2 reduction. The insertion of a pelletized sacrificial ZnO tetrapod scaffolding during aerogel synthesis resolves the mass transport problems present in other 3D aerogel-based catalysts. Further, the ZnO scaffolding allows for far easier nanoparticle loading as well as more facile adjustments to the aerogel's surface chemistry compared to a conventional aerogel made using standard methods.

Introduction

Traditionally, the energy used to enable and facilitate many chemical processes has been most commonly supplied through heat, either *via* combustion or electrical resistance. However, the past decade of research into photocatalysis has uncovered exciting benefits to harnessing energy from light. In this study, we focus on plasmonic photocatalysis where photochemical and photothermal mechanisms can both enhance reaction rates and selectivity compared to dark thermal processes.[1–18] Extensive research has delved into separating the two pathways,[12,17,19–35] understanding each on its own, and exploring how they can be combined for maximum synergy.[26,36–38] However, both mechanisms are hampered by the comparatively small illuminated volume that results when light shines upon a traditional catalyst bed. Further, the common use of powder-supported nanoparticles creates a highly heterogeneous reaction environment. Heat penetrates much deeper than light,[19,20,26] and as a result, a dark subsurface environment exists where only thermal mechanisms operate.[19,20,26] A common solution has been to use as thin a layer of catalyst as possible, however, the micron-deep optical penetration[21] of higher energy photons into a tightly packed catalyst bed makes this strategy imperfect, as well as imposing scale and mass flow limitations. These issues have prompted significant interest in the development of 3D monolithic structures for photocatalysis spearheaded by the Ozin group,[39–41] as well as by the Niederberger group specifically for aerogel-supported photocatalysts.[42–45] Expanding upon these and other studies,[46–50] we have created a highly porous 3D photonic monolith to support the plasmonic nanoparticle, whose unique optical design allows for the structure to be volumetrically illuminated. The plasmonic perspective gives specific attention to high temperature performance, the optical implications of loading the structure with plasmonic nanoparticles, and the importance of a readily tunable surface.

This work brings enhanced optical control to plasmonic photocatalysis, removing the heterogeneity caused by poor light penetration and the resulting differing reaction environments. Using an essentially transparent substrate gives the system designer more options to precisely control the optical distribution and observe the effects on rate and selectivity. The addition of a sacrificial template allows for further optical diffusion *via* multidirectional scattering and improves on a critical weakness of aerogels. Prior research has explored aerogels as metal particles supports due to their excellent optical qualities; however, the extremely fine pores of a traditional aerogel limit mass transport[45,51] and make its surface relatively inaccessible and difficult to modify. This can impede reaction throughput and the ability to modify the surface when attempting to tailor the aerogel surface chemistry for a specific

[a]*Duke University, Box 90346, Durham, North Carolina, USA. E-mail: j.liu@duke.edu*
[b]*NanoSYD, Syddansk Universitet, Campus Sonderborg, Alsion 2, Sønderborg, Denmark. Tel: +45 6550 7623*

reaction. Adjusting the aerogel reactor design can be effective at increasing mass transport[43] during the reaction but requires custom-built systems and does not allow for surface tunability. Thus, while optically promising, mass transport limitations present a hindrance for the performance and tunability of aerogel-supported photocatalysts. The novel photonic monolith presented herein addresses these mass flow limitations by introducing a microscale hierarchical network of interconnected channels *via* a sacrificial ZnO tetrapod scaffold.

This unique architecture not only unlocks better catalytic performance but also provides a dramatically more facile means to adapt the aerogel surface as desired. This article further explores the impact of this modification on optical properties and delves into the tradeoffs between optical, mass, and thermal transport for high temperature photocatalysts across a breadth of reaction conditions. The accompanying optical simulations visualize the extent to which the traditional illumination paradigm has been reshaped, and together with the optical characterization, they bring quantitative clarity to the degree of optical homogeneity now achievable for plasmonic reactions. Finally, the breadth of reaction conditions spotlights the potential sacrifices made to thermal performance for this burgeoning genre of plasmonic photocatalysts. Thus, this work explores a new 3D hierarchical architecture for high temperature photocatalysis, analyzes the nuanced changes to mass, optical, and thermal transport, and their combined effects on key metrics of catalytic reaction rate, selectivity, and efficiency. This paradigm shift from illuminated surface to illuminated volume opens new potential for high temperature photocatalysis, yet the wide-ranging implications and associated trade-offs have yet to be fully explored. This work reveals the impact of increasing support transparency on the catalytic function of plasmonic catalysts *via* adjustments to the nano- and micro-scale architecture and analyzes the nuanced effects on the competitive processes dictating reaction selectivity. Previous work on transparent monolithic catalysts, has presented novel catalysts, but has not directly compared them with more traditional powdered photocatalysts, examined the resulting shifts in reaction mechanisms due to increased transparency, or explored how these dynamics shift across a broad temperature range. In addition to these analyses, the pore-enhanced aerogel developed for this case study addresses challenges of reaction throughput and surface tunability of existing aerogel-based catalysts.

Results and discussion

The synthetic scheme for the Rh/SiO_2 pore enhanced aerogel (Rh/SiO_2-PEA) catalyst was inspired by a sacrificial ZnO tetrapod template strategy pioneered by Mishra *et al.*,[52,53] subsequently adapted by Schütt *et al.*[54] to produce an exceptional boron nitride optical diffuser, and then further developed to produce an "aeroglass" material.[55,56] This strategy was adopted due to the excellent scalability such that the molded catalysts can conform to an arbitrary reactor chamber, relatively mild reaction conditions and insensitive precursors, and micro scale porosity which enables simpler metal loading (surface functionalization not required). The micro-scale pores make the surface more accessible to reactants yielding more facile surface modification as well as enhanced reaction throughput. Essentially, a powder of microscale ZnO tetrapods, synthesized using the flame transport method, is pressed into a pellet to form an interconnected network of rods (Fig. 1a). Each ZnO tetrapod building block has a crystalline core with the extending arms separated at an angle of 105°. Heating the pellet solidifies the network by sintering the abutting arms of neighboring tetrapods. The porosity of the resulting microtube network exceeds 95%, enabling it to be easily loaded by simply drop casting a solution of Rh nanoparticles using a volume that nearly saturates the pellet. This strategy not only allows for easier loading of catalysts, but it also ensures the catalyst is concentrated along these passages. At this point, the surface can also be modified, such as by growing a thin film of TiO_2 (Fig. S1). Once the desired catalyst and coatings have been set on the scaffolding, a silicate precursor is briefly mixed with a gelation agent, aqueous ammonia, and added to a mold containing the loaded scaffold. By adding the gel solution before appreciable gelation begins, the gel forms around the loaded scaffold, adhering to its surface. Once set, the wet gel is then soaked in acid to remove the ZnO scaffolding. While the ZnO template is removed, the catalyst and coatings remain bound to the gel. Finally, the wet gel is dried in a critical point drier, yielding the final catalyst monolith (Fig. 1b). Specific details can be found in the materials and methods section along with a diagram in Fig. S2 and a TEM image in Fig. S3.

The channels induced by the sacrificial ZnO template were mapped by imaging a dyed wet gel using a confocal microscope. The resulting maps (Fig. 1c and d) indicated that the pore structure was consistent throughout the monolith. The data was analyzed using Imaris Microscopy Image Analysis software to form a 3D model (Fig. 1e). This analysis revealed that most of the channel network is interconnected. Thus, the modification to the monolith structure to accommodate mass transport was confirmed to be homogenous and contiguous. When compared to a pristine aerogel the mass flow rate was improved on average by 23% (Fig. S4). For this work, a single pellet density and tetrapod size were used, with only the concentration of the nanoparticle catalyst adjusted. However, adjusting the density of ZnO pellet, as well as tuning the tetrapod size, offers additional flexibility in balancing mass and optical transport.[52,54] Future work on further tuning pore size and density to understand the optimal balance between mass and photon transport could shed additional light on the ultimate utility and scalability of these promising 3D structures.

In addition to providing improved porosity, the ZnO tetrapod-based scaffolding also eases the burden of loading nanoporous aerogels with catalyst and modifying the aerogel surface. Catalyst loading requires no additional surface functionalization, and the nanoparticles are naturally positioned along the channels. Finally, the ZnO tetrapod scaffold provides an easily accessible surface where additional coatings

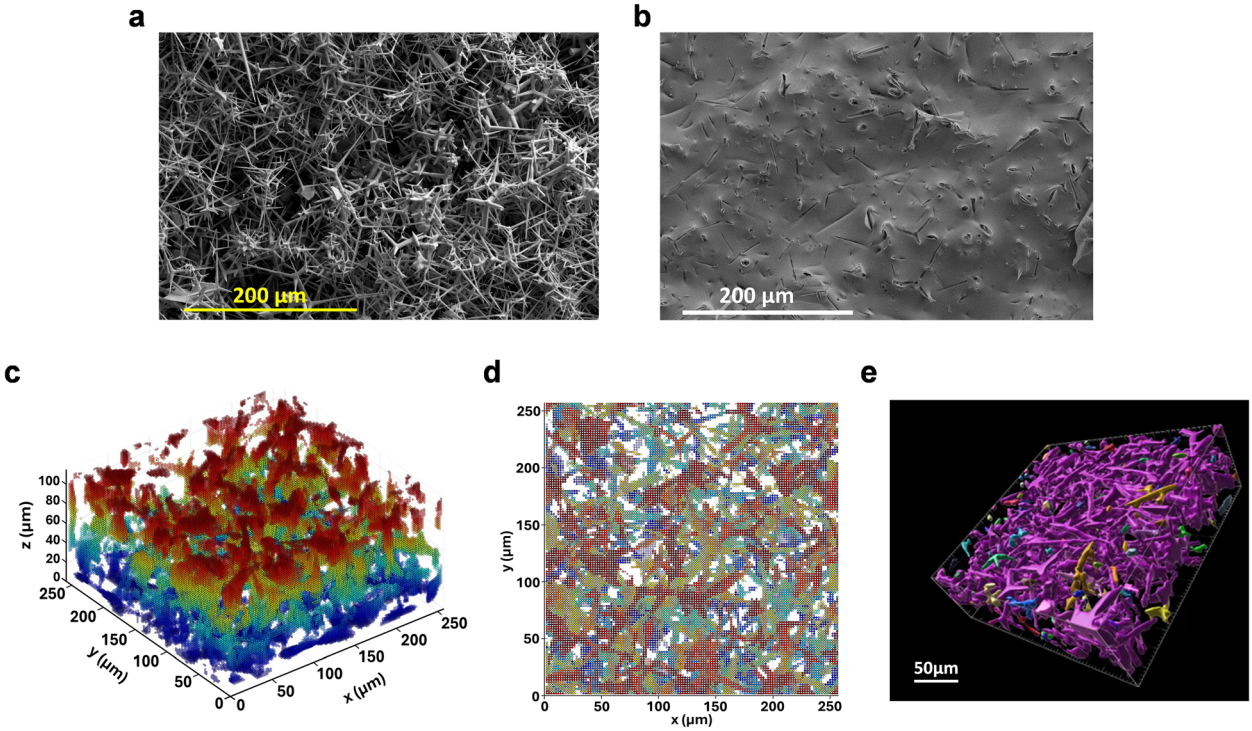

Fig. 1 Structural Characterization and Analysis. SEM images of (a) sacrificial ZnO tetrapod scaffolding, (b) Rh/SiO_2-PEA surface. Digitally reconstructed maps of channel structure in the Rh/SiO_2-PEA, where color denotes *z*-axis height from an (c) isometric and (d) top-down perspective. (e) Digital rendering of channel structure with color denoting interconnectivity. Data for the maps and rendering were collected using confocal microscopy.

can be readily applied to tune the surface chemistry. While a layer of TiO_2 was grown as a proof of concept for this article (Fig. S1), additional work on tuning the monolith surface chemistry for a specific reaction presents an exciting avenue of research for these 3D photocatalytic monoliths.

The performance of the novel Rh/SiO_2-PEA for photocatalytic CO_2 reduction was compared to two powdered Rh/SiO_2 catalysts with different loading schemes (Fig. 2). TEM images of the powdered catalysts can be found in Fig. S5. The reaction was performed under continuous Blue LED illumination and in a commercial reactor. While the plasmonic absorption of the Rh nanoparticles' peaks in the UV, blue was chosen to avoid potential absorption by the support structure, especially at higher temperatures, while still exciting the LSPR at the tail of the Rh particles' plasmonic absorption peak.[12,26,57] Absorbance spectrum of the Rh nanoparticles can be found in Fig. S6. Further details of the catalytic measurements can be found in the materials and methods section and a system diagram can be found in Fig. S7. Rh/SiO_2-PEA (Fig. 2a) was first compared to SiO_2 powder with a homogeneous 0.7 wt% Rh nanoparticle loading, termed Rh/S-POW-H (Fig. 2b). Several observations immediately stand out when comparing the two homogeneously loaded catalysts. Most significantly, the Rh/SiO_2-PEA is much more responsive to light than the traditional powder. CO production of Rh/SiO_2-PEA increases with light intensity at all tested reactor temperatures, 25–400 °C. However, the powdered Rh/S-POW-H is much less responsive to light and only begins to show activity when the reaction chamber is heated to 200 °C by the reactor's internal resistive heating element. Of these two homogenously loaded catalysts, the Rh/SiO_2-PEA outperforms the Rh/S-POW-H under all moderate to high light intensity (>2.5 W cm^{-2}). Yet, Rh/S-POW-H does outperform the aerogel-based catalyst under a single condition – in the dark at high reactor temperature. This is not surprising as aerogels are widely known to be among the best thermal insulators.[58–60] In additional to the well-known thermally insulating nature of the aerogel, the Rh catalyst nanoparticles in the aerogel monolith are further shielded from the heating of the reactor walls of the reactor, due to the gap between the rigid pellet and the metal sample cup. This poorer contact with the heated reactor, combined with the aerogels insulating properties results in inferior performance in dark thermal conditions. Thermal imaging of the aerogel and powder depicts how the flow of optical energy is improved over powder, but thermal flow from the reactor is sacrificed (Fig. S8). Accordingly, the performance of Rh/SiO_2-PEA is only weakly associated with reactor temperature, and almost exclusively determined by light intensity. By sacrificing thermal penetration for optical penetration, the Rh/SiO_2-PEA outperforms the powder supported catalyst with equivalent spatial distribution of catalyst under illumination.

To further explore the significance of 3D bulk illumination *versus* 2D surface illumination, the performance of Rh/SiO_2-PEA was compared to the performance of a powdered catalyst

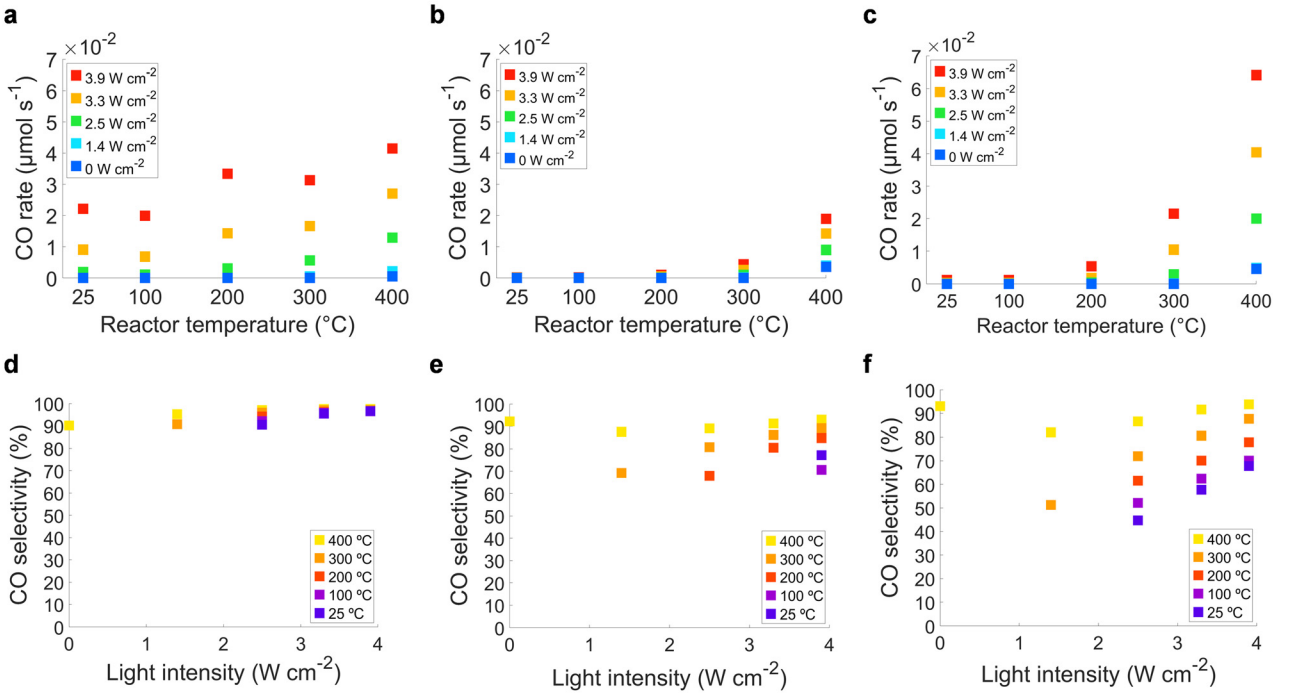

Fig. 2 CO_2 reduction on plasmonic Rh/SiO_2 photocatalysts. (a–c) CO production rates for (a) Rh/SiO_2-PEA (aerogel) catalyst with 0.7 wt% Rh loading, (b) Rh/S-POW-H (powder) Rh/SiO_2 catalyst with uniform Rh distribution, (c) "surface concentrated" Rh/S-POW-S catalyst made with a thin layer of higher wt loaded catalyst on top of bare SiO_2. The backfill of powder maintains an equal distance to the light source across samples. (d–f) CO selectivity for (d) Rh/SiO_2-PEA (aerogel), (e) Rh/S-POW-H powder Rh/SiO_2 catalyst with uniform Rh distribution, (f) Rh/S-POW-S catalyst with Rh concentrated at the surface. Temperatures are the reactor set temperature. In some low temperature/low brightness conditions, rection activity was insufficient to reliably calculate selectivity and was therefore excluded. All samples loaded with equal weight Rh and illuminated by a Blue LED centered on 455 nm.

where the Rh photocatalyst was more concentrated on the surface. This surface concentrated powdered catalyst is designated as Rh/S-POW-S (Fig. 2c). Whereas the Rh/S-POW-H distributed the Rh evenly throughout, the Rh/S-POW-S had all the Rh contained in a thin 7 mg layer sitting atop 13 mg pure SiO_2 powder. A total weight of 20 mg was maintained in both systems to ensure the same distance from the LED light sources, ensuring the incident light intensity remained comparable among all three samples. Among these samples, the Rh/S-POW-S exhibited a stronger but qualitatively similar relationship to both light and heat than the Rh/S-POW-H. As with the Rh/S-POW-H, it is only when reactor temperatures exceed 200 °C that enough catalyst is energized for the reaction to start and for a typical Arrhenius relationship to manifest with increasing reactor temperature. However, with a denser layer of surface-exposed catalyst, Rh/S-POW-S displays at least some measurable activity at the brightest intensities at all reactor temperatures.

The notion of concentrating the catalyst in as thin a layer as possible is a common practice in plasmonic catalysis and reflects longstanding recognition of how energy can and cannot flow through the catalyst bed. Catalysts should be positioned in a manner that is most accessible to the form of energy provided. The relatively permeable nature of powder to thermal energy dictates that proximity to the resistive heater at the bottom of the reactor should be sacrificed for proximity to the diverging light source that illuminates the top surface. In contrast, the novel Rh/SiO_2-PEA catalyst is more permeable to light than heat, upending this longstanding paradigm and creating new possibilities for high-temperature photocatalysis.

The indivisible nature of the monolith makes definitively attributing the reaction mechanism according to the best practices established in recent thermal/nonthermal plasmonic catalytic treatises[19,22,26,28,31,34,61] practically difficult. Still, observations of the reaction selectivity (Fig. 2d–f) combined with literature insight provide sufficient means to access the mechanisms within the broad introductory scope of this article. First, as mentioned previously, the blue illumination aligns with the tail of the plasmonic absorption peak. Thus, the frequency of illumination resonates relatively weakly with the particles' natural frequency, making it less likely that enough high-energy hot carriers are being generated and then injected into adsorbate orbitals to be the dominant driving force of the reaction. Second, across all samples, CO selectivity improves with increasing reactor temperature. This observation aligns with prior research on product selectivity in CO_2 hydrogenation over plasmonic Rh catalysts, suggesting CO is produced *via* a thermal mechanism.[12,21] In this mechanism, after dissociative adsorption of CO_2, CO desorbs thermally before it can be hydrogenated to CHO and experience hot

carrier-driven C-O bond scission.[12,21] A more detailed study of the reaction energetics for CO_2 evolution on plasmonic Rh nanoparticle catalysts can be found in ref. 12. The competing reaction mechanisms are outlined in Fig. S9. Based on experimental design, literature reports, and observed selectivity, the dominant mechanism is determined to be photothermal.

The selectivity data also reflects the trends observed with the reaction rate data. As with productivity, the selectivity in the aerogel is determined significantly more by optical conditions than by reactor heating. This is most dramatically apparent in conditions of lower reactor temperatures and higher light intensities. Conversely, the selectivity of powdered catalyst is much more responsive to the reactor's heat than the aerogel. As previously noted the thermally insulating character of the aerogel and poor contact with the reactor walls both prevent the nanoparticle from accessing the energy provided by the heater and inhibits the metal particles from conducting photothermal heat to and from the reactor body and to the external environment. We therefore hypothesize that under illumination, more of the photon's energy remains with the nanoparticles in the Rh/SiO_2-PEA than with the powdered catalyst. Further, thermographic and pneumatic measurements on related 3D photonic structures have demonstrated exceptional volumetric photothermal responses capable of heating internal gases to 300 °C in a matter of seconds under high light intensities.[55] Thus, at a given light intensity the nanoparticles as well as the reagent gases in the monolithic sample rapidly equilibrate to a higher temperature than those in the powders, giving superior photothermal catalytic rates and selectivity compared to traditional powders. The exothermic nature of CO_2 reduction reaction further compounds this effect as hot particles have higher turnover frequencies, generating more heat that cannot be efficiently dissipated. While heat buildup was likely an advantage for the aerogel sample for productivity and selectivity in this study, it could prove deleterious in other contexts and deserves more detailed study. While homogenizing the reaction conditions leads to a more uniform product distribution for this reaction, it is imperative for future studies to consider these nuances when attributing the primary catalytic mechanism. Future studies where the monolith surface and experimental design have been tuned to favor photochemical products[12] could provide valuable insight into this critical balance.

To understand the Rh/SiO_2-PEA's enhanced response to illumination, optical measurements were performed in a lab constructed haze meter (Fig. S10). Optical characterization presented in Fig. 3a illustrates the efficiency of optical transmission of a standard aerogel, pore enhanced aerogel (PEA) and Rh

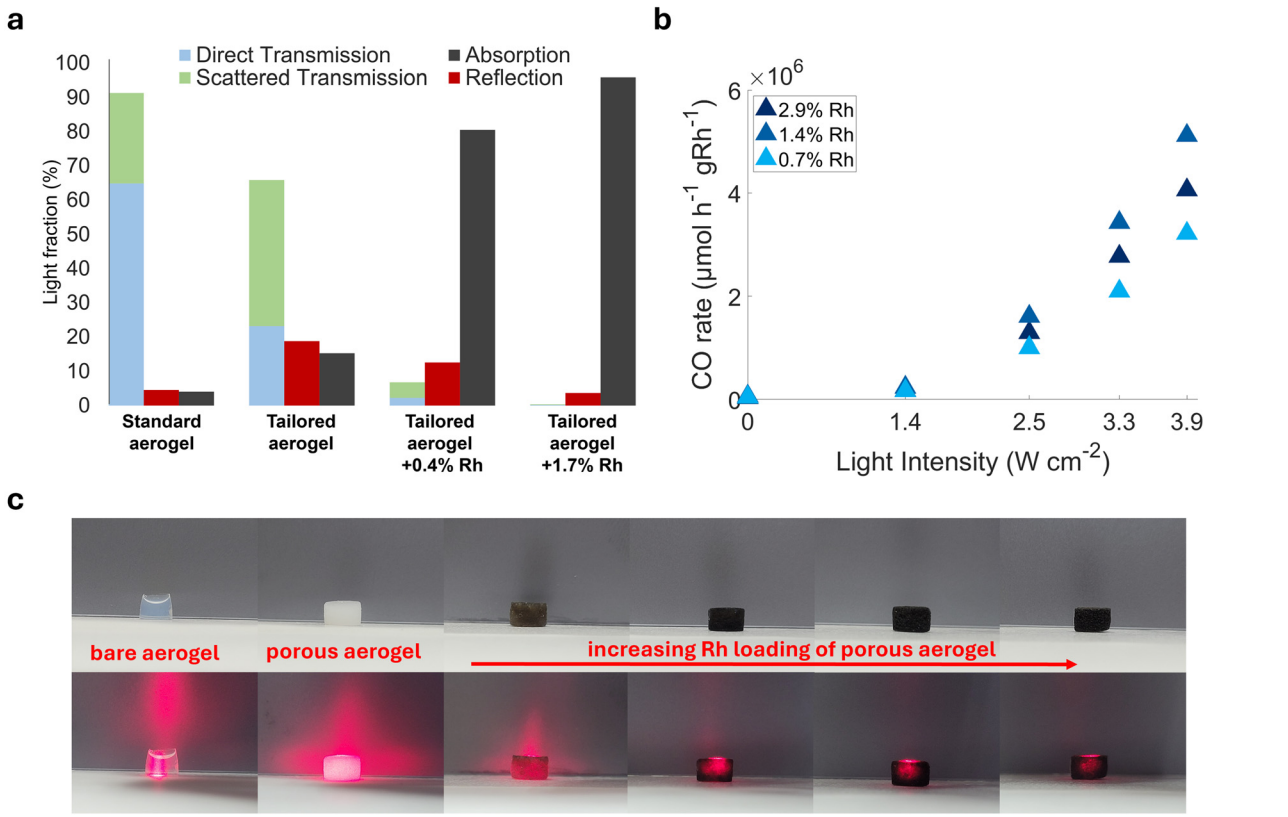

Fig. 3 Optical properties and implications for catalyst loading. (a) Optical measurements of aerogel structures performed with 532 nm laser and an integrating sphere. Measurement procedure is detailed in the methods section and Fig. S7. (b) CO production adjusted for amount of Rh used. Illuminated by a Blue LED centered on 455 nm, reactor temperature set to 400 °C. (c) Qualitative images of aerogel-based samples in ambient lighting and illuminated by a red laser pointer.

loaded PEA. The standard aerogel has low losses, which could be further improved by reducing reagent concentration during synthesis. This would in principle improve the optical performance of the pristine material by reducing the aerogels native pore and particle size at a cost to speed of synthesis.[59,62,63] Tailoring the amount and size of pores is a critical aspect of monolithic photocatalyst design. Pores are essential for mass transport, however, they are a detriment to optical transport. The tight pores of pristine aerogel are known to restrict mass flow in aerogel supported catalyst,[45,51,64] limiting the overall catalytic potential. Therefore, a network of interconnected channels was added to the aerogel to create the pore enhanced aerogel (Fig. 3a). This enhancement of mass transport came at a notable increase in energy loss both due to the support absorbing more light, a result of increased path length, and an increase in reflection of light towards the source. Combined optical loss quadrupled from a combined 8.6% to 34.1%. Serendipitously, loading the structure with plasmonic particles reversed the increased losses, restoring the system's optical efficiency. Upon the addition of only 0.4 wt% Rh nanoparticles, loss to reflection decreased from 18.8% to 12.6% (Fig. 3a). All aerogel loadings had significantly reduced reflection compared to both the lower and higher powders controls which were 35% and 17% respectively (Fig. S11). Reducing reflection is a key benefit of these structures, especially at lower metal loadings often used to avoid particle agglomeration. Maximizing metal surface area is of particular concern given the rare and expensive nature of plasmonic metals. The dramatic reflection reduction of the pore tailored aerogel is well positioned to maximize the cost efficiency of the plasmonic metal. Increasing the loading to 1.7 wt% further decreased reflection loss to only 3.7%. Increasing the loading also reduced the amount of energy exiting the system due to photons passing through the sample without being absorbed. For the 0.7 wt% loaded sample 6.8% of the incident photons went unused due to combined direct and scattered transmission. Increasing the Rh load to 1.7 wt% reduced these transmission losses to a mere 0.37%. Thus, increasing the loading led to the PEA catalyst capturing 95.9% of the incident optical energy.

These promising optical measurements prompted a study of the influence of Rh loading on catalytic effectiveness shown in Fig. 3b. Initially, adding more Rh improved performance as additional Rh not only provided more active sites, but also reduced losses to reflection. However, increasing Rh content beyond 1.7 wt% loading showed a diminishing increase in productivity. With 95.9% of the optical energy already being captured, there was rapidly diminishing potential energetic gains and simultaneously, increasing loading would decrease average optical penetration, resulting in catalyst being added to an increasingly dark environment.

To further understand how the 3D photonic design dictates the distribution of light throughout the catalyst, the internal optical environment was simulated using raytracing (Fig. 4). An effective refractive index approximation, incorporating scattering and absorption lengths extracted from the optical data presented in Fig. 3a enabled the simulation of the volumetric distribution of light within the unloaded and loaded PEA monoliths. Measurements of the optical dispersion and inten-

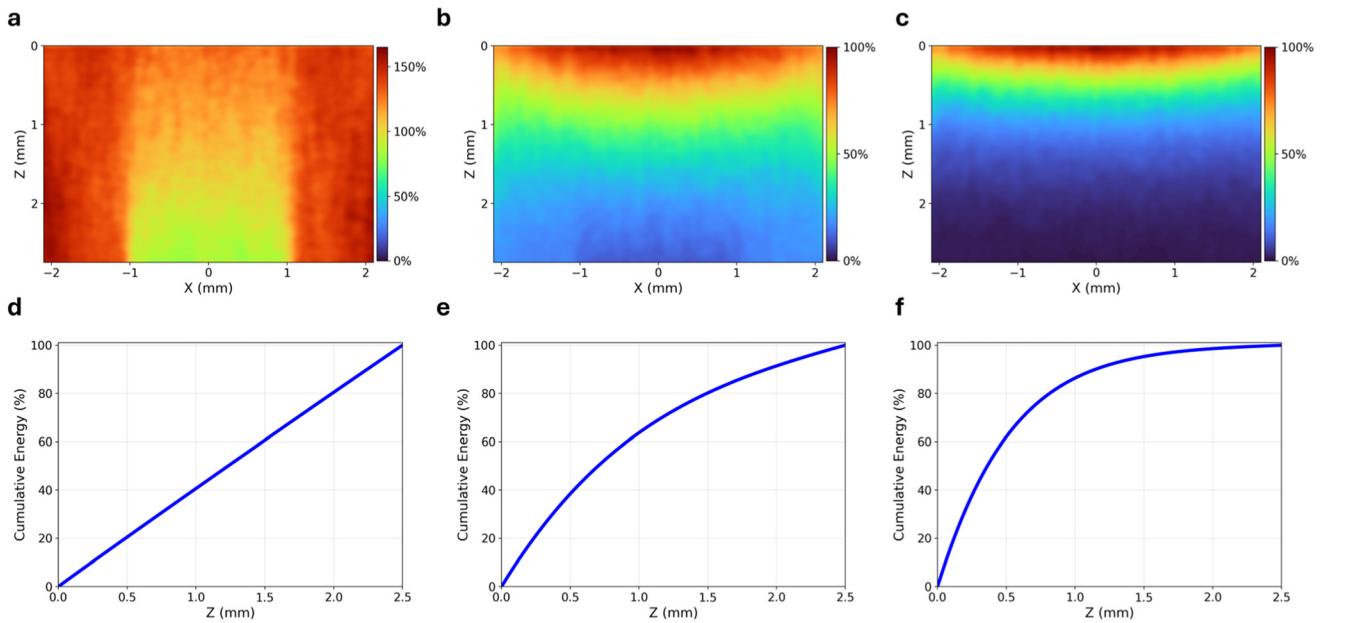

Fig. 4 Optical simulations and energy accumulation. (a–c) Raytracing simulations of (a) unloaded pore enhanced aerogel. Note that the increased illumination of the sides is due to reflection off the sample chamber floor compared to the center region which extends across the 2 mm wide gas outlet, (b) pore enhanced aerogel with 0.4 wt% loading Rh, (c) pore enhanced aerogel with 1.7 wt% loading Rh. In (a), intensity exceeds 100% in certain regions due to reflection from the walls and floor of the reaction chamber. (d–f) Simulated energy accumulation normalized to total absorption of the sample for (d) unloaded pore enhanced aerogel, (e) pore enhanced aerogel with 0.4 wt% loading Rh, (f) pore enhanced aerogel with 1.7 wt% loading Rh.

sity allowed for light source of the simulation to accurately match the LED light source used for catalysis. More details on the simulation methodology can be found in the materials and methods section. Fig. 4a shows the unloaded pore enhanced aerogel. Light penetrates deeply and the entire structure is brightly illuminated. As result of the optical divergence and subsequent reflection off the reactor walls and floor, a large portion of the interior volume experiences intensity greater the initial illumination. Only the portion of the monolith atop the reactor outlet experiences less than 100%, with the bottom of the monolith receiving <75% illumination, in good agreement with the experimental measurements.

Simulation of the lightly loaded 0.4 wt% Rh PEA monolith revealed a broad and deep gradient of illumination that extended through the entirety of the bulk (Fig. 4b). The penetration depth of light was increased several orders of magnitude compared to calculations of light penetration into powdered catalyst.[21] The broad intensity gradient across the monolith volume suggests that changes to metal loading and illumination scheme to create a uniformly illuminated catalyst monolith are a possible and exciting direction for future work. The optical environment could be further homogenized either by decreasing loading across the entirety of the monolith or restricting catalyst towards regions with sufficiently bright illumination. By decreasing the volume of Rh solution added to significantly below the saturation limit, the depth of catalyst distribution can be easily tuned to regions with sufficiently bright illumination *i.e.* not less 50% surface intensity. Thus, these 3D photonic structures provide an accessible means to ensure bright illumination across all catalyst particles, eliminating the dual reaction zone paradigm[19,20,26] that has thus far hampered selectivity and scalability in high temperature photocatalysts with both thermal and nonthermal activities.

Creating a more uniformly illuminated environment across a catalyst volume with poor thermal transport could further assist the study of the thermal vs nonthermal, *i.e.*, photothermal vs photochemical mechanisms in plasmonic catalysis. Understanding the relative contributions of photothermal and photochemical reaction mechanisms has been a subject of extensive research. However, these studies are complicated by the heterogeneous thermal and optical environment created when light shines upon a powder.[19,20,26] Prior research, embracing the heterogeneity of the reaction environment, has yielded some clarity on this balance.[26] Now, by turning to a monolithic design, the contrasting environments of illuminated surface and dark subsurface can be obviated. 3D photonic structures can provide a more homogeneous environment, which can direct selectivity towards a single product.

The highly heterogeneous illumination of powdered catalysts can be particularly problematic when dark thermal activity produces an alternative product compared to the photoproduct of the exposed surface. Some researchers have circumvented this conundrum by developing catalysts with negligible thermal activity.[1] However, homogenizing the reaction environment using a 3D photonic monolith presents an alternative path to improving product selectivity.

Fig. 4c depicts the PEA catalyst with a higher 1.7 wt% Rh loading, resulting in a steeper gradient of illumination. This aligns well with the observed decrease in efficiency of 2.9 wt% loaded catalyst compared to the 1.4 wt% load in Fig. 3b. When added uniformly across the monolith, only a fraction of the catalyst added beyond 1.7 wt% loading of Fig. 4c, would receive meaningful illumination. Continuing to add catalysts would make the gradient even more dramatic until its bulk optical profile was similar to that of powdered catalyst, albeit with poorer thermal conductivity. Thus, these simulations and measurements provide a useful framework for optimizing the catalyst for monolithic catalyst supports.

From these simulations, the energy accumulation across the depth of the structure was calculated and plotted (Fig. 4d–f). The plot provides a more quantitative visualization of how energy is distributed within the 3D photonic structure. For an unloaded aerogel monolith, nearly 85% of light passes through (Fig. 3a). The 15% that remains within the structure forms a homogenous energy distribution environment. Each vertical "slice" in the axis of illumination is in a comparable environment of optical excess. However, loading the monolith with strongly absorbing plasmonic particles (Fig. 4e and f) results in energy accumulation, which follows an exponential cumulative distribution function

$$\text{Cumulative optical energy}(x;\lambda) = 1 - e^{-\lambda x}$$

where x is the depth along the axis of illumination and λ is the rate parameter, which is determined by the nanoparticle loading. Increasing the catalyst loading shifts the cumulative energy distribution in line with an increase in the rate parameter λ and improves the fit to the cumulative distribution function model (Table S1). This aligns well with the nature of optical absorption across a sample with a random distribution of absorbers. In this system, optical absorption is a Poisson process. As light travels through the monolith, the increasing path length makes it increasingly likely that it will have encountered a metal particle and been absorbed, however, each individual potential absorption event remains independent of all others and the path the photon has traveled. As more nanoparticles are added, the rate parameter λ, indicating the time/distance between Poisson events, increases, corresponding to a shorter time/distance between absorption events (Table S1).

Theoretically, two factors may shift the optical behavior of the monolith away from a Poisson model. The first is inelastic scattering. However, while Raman scattering is significant for sensing applications, the relative rarity of Raman scattering events allows it to be ignored when discussing photocatalytic production. Second and more significant are temperature-dependent effects on the nanoparticles' localized plasmon resonance (LSPR).[65] Photothermal heat from intense light, as well as heat released by exothermic reactions, can increase the temperature of the plasmonic metal particle. Changes in the nanoparticle temperature can have complex effects on its LSPR, influencing both plasmonic absorption peak position

and intensity.[65] Factors such as lattice expansion, shifts in the population distribution of occupied states, and degradation of polarizability due to thermal oscillations are among the temperature dependent known to significantly influence the LSPR.[65] Additionally, these factors impact both optical absorption and scattering and are highly dependent on the elemental metal as well as the particle size and morphology. Thus, under higher illuminating intensities, particles at the surface may have a decreased absorption cross-section than particles deeper in the monolith. It is important to note that the optical measurements upon which the simulation was based were conducted at room temperature using a green laser. The differences between the environment in which the optical characterization was performed and the environment in which the catalysis occurred necessarily create some discrepancies. However, while the environments were not identical, the trends in the data of both optical and catalytic experiments align well. The agreement between the loading dependence of the structure's optical profile (Fig. 3a) and catalytic efficiency (Fig. 3b) asserts the relevance of the optical measurements to the catalytic phenomena.

Thus, while the optical measurements and derived simulation are *ex situ*, they still provide valuable insight into the novel optical properties of the monolithic photocatalyst. A future study systemically adjusts the height and loading of the samples across a breadth of different nanoparticle absorbers, and temperatures could provide data necessary for a more expansive predictive energy distribution model. Such a model could rapidly accelerate the adoption of monolithic photocatalyst by ubiquitously providing a highly informed starting point for the otherwise tedious process of optimizing catalyst loading to the volume for a given reactor volume, nanoparticle optical cross-section, and illumination scheme.

This optical characterization, simulation, and analysis should be viewed in the context of the structural-optical property relationship of aerogels and how they differ from traditional powders.[59,62,63] Aerogels are composed of tiny nanoparticles (significantly smaller than light's wavelength), which cause only weak Rayleigh scattering, allowing light to mostly pass through. However, the larger particles common to most powders cause strong Mie scattering, rapidly diffusing light, and making the support material opaque. Additionally, the aerogel's porous structure has a low refractive index, close to air, minimizing scattering at interfaces compared to the powder's dense packing, which creates a high refractive index contrast with air, increasing scattering. Finally, aerogel's open network reduces interfaces where light scatters, whereas powders' tightly packed particles increase scattering. Absorption is negligible in both cases, so the key difference between aerogel and powders comes from scattering and refractive index effects. Thus, pristine aerogel generally appears translucent with a faint blue color, while powder appears opaque and white. Therefore, from an optical perspective, aerogel is a superior support for photo-driven processes occurring across a bulk volume. While optically designed 3D monolithic catalysts hold exciting promise for both photothermal and photochemical processes, their greatest potential application may be for reactions with photochemical mechanisms. Since the photochemical pathway only emerges under direct light illumination, it would stand to reason that photochemical rates would receive greater benefit from the optical environment provided by these 3D monolithic structures. However, it is important to consider the thermal impact of aerogel as well. Greater thermal accumulation due to decreased thermal conductivity could spur thermal rates faster than the plasmonic process can provide excited carriers, potentially outpacing the increase in photochemical reactivity.

Conclusion

This article provides a greater understanding of and novel solution to the challenging balance between energy and mass transport inherit to heterogenous photocatalysis. We demonstrate a facile approach to circumvent mass flow limitations in standard aerogels. Serendipitously, the ZnO scaffolding architecture that is employed to solve the mass transport challenges also provides a more facile method of catalyst loading and surface modification. Additionally, this article highlights the effects on bulk optical properties incurred when augmenting mass transport as well as quantifying the implications of incorporating increasing amounts of strongly light-absorbing photocatalyst. The methods presented here provide a blueprint for striking the optimal balance between energy and mass transport, two essential properties of heterogenous photocatalysis, and a more informed starting point for others seeking to leverage this technology. The optical measurements and simulation support the analysis, provide quantitative visualization of the optical enhancements and showcase how the distribution of photons can be readily tuned across a 3D monolith. Finally, this article advances the field of monolithic photocatalysts with detailed attention to the unique implications for high-temperature processes. The breadth of high-temperature photocatalytic data provided herein highlights the unique relationships between thermal and optical energy transport for highly porous monoliths with isolated absorbers. Table S2 compares the photocatalytic monolith in this work to those of other works.

In conclusion, a new monolithic plasmonic photocatalyst was synthesized, and its physical and chemical nature was analyzed. The 3D photonic structure created a dramatically different paradigm for high-temperature photocatalysis whereby all catalyst nanoparticles throughout the bulk volume can be illuminated. Rh nanoparticles operating in this paradigm exhibited a greatly enhanced catalytic response to light, but a more limited response to conducted heat. This resulted in a greatly enhanced reaction rate and selectivity when the reactor was brightly illuminated absent supplemental heat. This enhanced photo response provides exciting potential for the field of plasmonic catalysis as well as for the broader study of heterogeneous photocatalysis.

Materials and methods

Synthesis

Rh nanoparticles. Rh nanoparticles were synthesized according to published polyol methods.[12,21,26] 25 mg Polyvinylpyrrolidinone (PVP ~ w. 55 000) was dissolved in 10 ml ethylene glycol at 160 °C under vigorous stirring in a round bottom flask. Separately, 24 mg $RhCl_3$ hydrate (~35–40 wt% Rh) was dissolved in 0.8 ml ethylene glycol. The Rh solution was quickly injected into the hot PVP solution and stirred for 30 minutes at 160 °C. After cooling to room temperature, the solution was washed with acetone and then water/acetone twice. First, the reaction mixture was diluted to 30 ml with acetone, divided into fourths, sonicated, centrifuged, and the supernatant discarded. The sediment in each tube was resuspended in a minimal amount of DI H_2O (~1 ml) and then diluted to 8 ml with acetone and sonicated. After two water/acetone washes the final product was suspended in EtOH at concentrations of 1.5–2 mg ml^{-1} and stored in freezer at −17 °C.

Sacrificial ZnO microrod template. ZnO tetrapods were synthesized by flame transport synthesis procedure.[52,53] Zn powder (diameter ~ 5 μm) is mixed with polyvinyl butyral (PVB) in a 1 : 2 wt ratio in a ceramic crucible. The crucible is then placed in a preheated (450 °C) muffle furnace. The furnace temperature is then increased to 900 °C. The furnace remained at 900 °C for 30 minutes and then cooled naturally resulting in the growth of micro- and nanoscale ZnO tetrapods structures. In flame transport synthesis process, the tetrapod growth occurs *via* solid-vapor-solid process in flame controlled ambient conditions. This tetrapod production process by flame synthesis is scalable and is commercially available. The tetrapods are collected and for each pellet 20 mg is pressed in a mold 3 mm in height and 5 mm in diameter. The pellets are then further heated at 1150 °C for 5 hours yielding highly porous interconnected ZnO tetrapods network as sacrificial template to create the 3D monolithic network.

Catalyst loading. 55–60 μl Rh nanoparticle solution was drop cast onto the top of the ZnO pellet such that it penetrated almost to the bottom of the pellet. After drying the pellet was flipped over and Rh solution was added to the opposite side. Rh loading was varied by adjusting the number of repetitions and the concentration of the Rh solution. After drying at room temperature, the Rh loaded ZnO pellets were calcinated at 400 °C in an open tube furnace.

Pore enhanced aerogel. Aerogel was synthesized following a Stober[66] style sol–gel method.[67,68] 1 ml of tetramethyl orthosilicate was added to 1 ml of methanol at room temperature while stirring. Separately, 0.4 ml 85.4 mM NH_3(aq) was added to 1 ml of methanol stirring at room temperature. The ammonia solution was then rapidly added to the silicate solution and stirred for 2 minutes at room temperature. After two minutes, 55 μl of gel solution was added to a mold containing the Rh-loaded ZnO pellet. The solution was left to gel for two hours while sealed and then immersed in 10 ml 1.2 M HCl overnight to remove the ZnO template. After etching, the wet monolith was placed in EtOH, and the EtOH was replaced daily for 5 days to exchange the solvent. Finally, the washed wet monolith was dried in a Tousimis Autosamdri-931 critical point drier.

Powdered catalyst. Powder silica support was synthesized using the Stober method.[66,69] 1 ml tetraethyl orthosilicate was added to 50 ml of Ethanol under vigorous stirring at room temperature. 3 ml 10.5 M NH_3(aq) was added, and the reaction mixture was stirred for 6 hours at room temperature. The product was washed three times with ethanol and then dried. The dried silica was ground and added to 100 ml of ethanol. While stirring, diluted Rh nanoparticle solution was added to the stirring silica slurry and the heat was increased to 200 °C. The solution was stirred until all the ethanol evaporated. The loaded silica powder was then calcinated in air at 400 °C and then ground.

Characterization

Optical characterization. Samples were characterized in a Thor Labs general-purpose ∅50 mm integrating sphere with a custom-made sample holder and illuminated by a 530 nm laser. Changing the beam path allowed total intensity, total transmission, scattered transmission, and reflectance to be individually measured and normalized. From these measured values, the absorbance and direct transmission were calculated. The measurement scheme is illustrated in SI Fig. S7. Absorption of Rh nanoparticles was measured in Shimadzu UV-3600i spectrophotometer.

Reflectance of powdered samples was measured in the same spectrophotometer using an integrating sphere attachment.

Structural characterization. SEM images were captured using an FEI (Thermo Fisher Scientific) Apreo S scanning electron microscope. The sample was contained in a custom made sample holder. TEM images were collected in an FEI Tecnai G^2 Twin as well as in a Thermo Scientific Talos F200X.

Confocal microscopy and porosity mapping. Confocal microscopy was used to investigate the connectivity of the pores in the aerogel sample. The sample was first dyed using a commercially available fluorescent dye. The sample was first dyed using a commercially available fluorescent dye (Rhodamine B) prepared at a concentration of 0.01 mmol. The dyed sample was then placed in a sample holder filled with 100% ethanol, ensuring that the sample was fully immersed in the solvent. The sample holder had a bottom thickness of 0.13 mm, which was compatible with high-resolution microscopy. The sample holder was then mounted on an inverted confocal microscope and a 514 nm laser as the excitation source. A 20× magnification objective lens with a numerical aperture (NA) of 0.70 was used to illuminate the sample and to collect the photoluminescence signal. The emitted photoluminescence signal was collected, and the spectral window of 700–780 nm was selected for detection to isolate the relevant emission signal. The spatial resolution for the measurement was set to 0.13 μm in both the *xy*-plane and the *z*-plane, ensuring high-resolution imaging of the sample.

The Aerogel structure was coated with fluorescent dyes, while the pores remained unfilled, creating a contrast in photoluminescence signals between the two regions under uniform illumination. The dark regions correspond to the unfilled pores, whereas the bright regions represent the dye-coated aerogel matrix.

The confocal microscopy data were analyzed using Imaris software (Bitplane, Zurich, Switzerland) to construct three-dimensional (3D) models and evaluate the connectivity of the poles in the Aerogel sample. To ensure consistency in intensity values across all z cross-sections, the intensity distribution of each z cross-section was normalized. The pixel intensity values were rescaled to fall within the range of 0 to 255. To emphasize positions of the poles in the original dataset, the normalized intensity values were inverted. This transformation converted dark regions into bright regions, enabling their visualization and analysis as high-intensity features. The inverted intensity dataset was imported into Imaris software, where a 3D model was constructed. The bright regions in each z cross-section were identified and used to generate a 3D reconstruction of the sample. Imaris's surface rendering algorithm was employed to visualize the spatial organization of the bright regions and assess their connectivity. The connected bright regions in the 3D model were segmented and assigned unique labels using Imaris's built-in segmentation tools. Each connected region was automatically labeled with a distinct color, facilitating visualization and analysis of the connectivity of the poles.

Simulation

We created our ray-tracing simulations for the aerogel samples with the help of an open-source Python-based photon path-tracing code (pvtrace), which we adapted to account for reabsorption and rescattering processes within the aerogel as well as reflection from mirrored walls with zero absorption. For each sample, we launched 10 million rays to capture the spatial intensity distribution, with intensity in each three-dimensional voxel defined by the number of rays passing through it. We used a 210 × 210 × 185 voxel grid (in x, y, and z, respectively) and matched the actual aerogel dimensions (cylinders with 4.2 mm diameter and 2.5 mm depth). To replicate our experimental setup, in which an LED-based laser source is delivered by a 5 mm-diameter liquid light guide, we initialized the rays at a 4.6 mm distance from the aerogel surface with a uniform radial distribution and used an 11 mm-diameter Gaussian profile to illuminate the sample.

The aerogel medium was modeled with an effective refractive index approximation, incorporating scattering and absorption lengths (L_s, L_a)[1] that were derived from measured transmittance (T), reflectance (R), and absorptance (A) values obtained *via* integrating sphere measurements.[2] Specifically, the attenuation length $L_{att} = -L/\ln T$, the absorption length $L_a = -L/\ln \mathrm{TF}$ with transflectance TF = 1 − A, and the scattering length $L_s = (L_{att}\, L_a)/(L_a - L_{att})$. Here L is the 2.5 mm thickness of the aerogel. We validated the model by comparing simulated and measured values of T, R, and A. For instance, for the unloaded pore enhanced sample, the measured values (T = 0.66, R = 0.19, A = 0.15) were in good agreement with those from the simulation (T = 0.69, R = 0.14, A = 0.17). Additionally, we incorporated surface roughness by using confocal microscopy to measure the three-dimensional topography of the aerogel and encoding the resulting distribution of surface normal into the reflection and scattering events at the air–aerogel interface.

Catalysis

Catalytic experiments were performed in a Harrick Raman high temperature reaction chamber according to previously described procedures.[12,19–21,26,36] The catalyst was pretreated with 50% H_2/Ar at 400 °C for 2 h. After cooling down, the feed was switched to 6 sccm CO_2, 24 sccm H_2 and 30 sccm Ar. The reactor temperature was set using a thermocouple inserted into the reactor between the heating element and reaction chamber. At each temperature set point (25, 100, 200, 300, 400 °C), the voltage of the 450 nm Prizmatix fiber optic LED was increased incrementally from 0–4.8 V resulting in calibrated light intensities of 0–3.9 W cm^{-2}. Outlet gas stream was fed directly to an International Crystal Laboratories FTIR gas cell and analyzed using a Thermo Fisher Nicolet 380 FTIR.

Conflicts of interest

There are no conflicts to declare

Data availability

The data supporting this article have been included as part of the supplementary information (SI). Supplementary information is available. See DOI: https://doi.org/10.1039/d5nr04370k.

Acknowledgements

This work was partially supported by the National Science Foundation (grant number CHE-1954838). It was performed in part at the Duke University Shared Materials Instrumentation Facility (SMIF), a member of the North Carolina Research Triangle Nanotechnology Network (RTNN), which is supported by the National Science Foundation (award number ECCS-2025064) as part of the National Nanotechnology Coordinated Infrastructure (NNCI). Additional support from the Duke Office for Climate and Sustainability is also gratefully acknowledged.

This work was also performed in part at the Chapel Hill Analytical and Nanofabrication Laboratory, CHANL, a member of the North Carolina Research Triangle Nanotechnology Network, RTNN, which is supported by the National Science Foundation, Grant ECCS-1542015, as part of the National Nanotechnology Coordinated Infrastructure, NNCI.

This work was supported by funding from the Duke Science and Technology Launch Seed Grant Program.

NML acknowledges NSF ECCS-2240562 Award.

YKM acknowledges the funding from the ESS lighthouse on hard materials in 3D, SOLID (Danish Agency for Science and Higher Education, grant number 8144–00002B), Denmark, NANOCHEM (national infrastructure UFM 52290-00010B, NANOCHEM, Denmark).

References

1 Y. Yuan, L. Zhou, H. Robatjazi, J. L. Bao, J. Zhou, A. Bayles, L. Yuan, M. Lou, M. Lou, S. Khatiwada, *et al.*, Earth-abundant photocatalyst for H_2 generation from NH_3 with light-emitting diode illumination, *Science*, 2022, **378**(6622), 889–893, DOI: 10.1126/science.abn5636.

2 E. Cortés, Activating plasmonic chemistry, *Science*, 2018, **362**(6410), 28–29, DOI: 10.1126/science.aav1133.

3 C. Zhan, Q.-X. Wang, J. Yi, L. Chen, D.-Y. Wu, Y. Wang, Z.-X. Xie, M. Moskovits and Z.-Q. Tian, Plasmonic nanoreactors regulating selective oxidation by energetic electrons and nanoconfined thermal fields, *Sci. Adv.*, 2021, **7**(10), eabf0962, DOI: 10.1126/sciadv.abf0962.

4 X. Wan, Y. Li, Y. Chen, J. Ma, Y.-A. Liu, E.-D. Zhao, Y. Gu, Y. Zhao, Y. Cui, R. Li, *et al.*, A nonmetallic plasmonic catalyst for photothermal CO2 flow conversion with high activity, selectivity and durability, *Nat. Commun.*, 2024, **15**(1), 1273, DOI: 10.1038/s41467-024-45516-4.

5 L. Zhou, J. M. P. Martirez, J. Finzel, C. Zhang, D. F. Swearer, S. Tian, H. Robatjazi, M. Lou, L. Dong, L. Henderson, *et al.*, Light-driven methane dry reforming with single atomic site antenna-reactor plasmonic photocatalysts, *Nat. Energy*, 2020, **5**(1), 61–70, DOI: 10.1038/s41560-019-0517-9.

6 Y. Yuan, J. Zhou, A. Bayles, H. Robatjazi, P. Nordlander and N. J. Halas, Steam methane reforming using a regenerable antenna–reactor plasmonic photocatalyst, *Nat. Catal.*, 2024, **7**(12), 1339–1349, DOI: 10.1038/s41929-024-01248-8.

7 D. Devasia, A. J. Wilson, J. Heo, V. Mohan and P. K. Jain, A rich catalog of C–C bonded species formed in CO_2 reduction on a plasmonic photocatalyst, *Nat. Commun.*, 2021, **12**(1), 2612, DOI: 10.1038/s41467-021-22868-9.

8 F. Lin, B. Shao, Z. Li, J. Zhang, H. Wang, S. Zhang, M. Haruta and J. Huang, Visible light photocatalysis over solid acid: Enhanced by gold plasmonic effect, *Appl. Catal., B*, 2017, **218**, 480–487, DOI: 10.1016/j.apcatb.2017.06.076.

9 U. Aslam, V. G. Rao, S. Chavez and S. Linic, Catalytic conversion of solar to chemical energy on plasmonic metal nanostructures, *Nat. Catal.*, 2018, **1**(9), 656–665, DOI: 10.1038/s41929-018-0138-x.

10 B. Xie, R. J. Wong, T. H. Tan, M. Higham, E. K. Gibson, D. Decarolis, J. Callison, K.-F. Aguey-Zinsou, M. Bowker, C. R. A. Catlow, *et al.*, Synergistic ultraviolet and visible light photo-activation enables intensified low-temperature methanol synthesis over copper/zinc oxide/alumina, *Nat. Commun.*, 2020, **11**(1), 1615, DOI: 10.1038/s41467-020-15445-z.

11 S. Singh, R. Verma, N. Kaul, J. Sa, A. Punjal, S. Prabhu and V. Polshettiwar, Surface plasmon-enhanced photo-driven CO_2 hydrogenation by hydroxy-terminated nickel nitride nanosheets, *Nat. Commun.*, 2023, **14**(1), 2551, DOI: 10.1038/s41467-023-38235-9.

12 X. Zhang, X. Li, D. Zhang, N. Q. Su, W. Yang, H. O. Everitt and J. Liu, Product selectivity in plasmonic photocatalysis for carbon dioxide hydrogenation, *Nat. Commun.*, 2017, **8**(1), 14542, DOI: 10.1038/ncomms14542.

13 D. F. Swearer, H. Zhao, L. Zhou, C. Zhang, H. Robatjazi, J. M. P. Martirez, C. M. Krauter, S. Yazdi, M. J. McClain, E. Ringe, *et al.*, Heterometallic antenna–reactor complexes for photocatalysis, *Proc. Natl. Acad. Sci. U. S. A.*, 2016, **113**(32), 8916–8920, DOI: 10.1073/pnas.1609769113.

14 H. Sheng, J. Wang, J. Huang, Z. Li, G. Ren, L. Zhang, L. Yu, M. Zhao, X. Li, G. Li, *et al.*, Strong synergy between gold nanoparticles and cobalt porphyrin induces highly efficient photocatalytic hydrogen evolution, *Nat. Commun.*, 2023, **14**(1), 1528, DOI: 10.1038/s41467-023-37271-9.

15 E. Schroeder and P. Christopher, Chemical Production Using Light: Are Sustainable Photons Cheap Enough?, *ACS Energy Lett.*, 2022, **7**(2), 880–884, DOI: 10.1021/acsenergylett.2c00142.

16 Y. Kim, J. G. Smith and P. K. Jain, Harvesting multiple electron–hole pairs generated through plasmonic excitation of Au nanoparticles, *Nat. Chem.*, 2018, **10**(7), 763–769, DOI: 10.1038/s41557-018-0054-3.

17 A. Stefancu, N. J. Halas, P. Nordlander and E. Cortes, Electronic excitations at the plasmon–molecule interface, *Nat. Phys.*, 2024, **20**(7), 1065–1077, DOI: 10.1038/s41567-024-02537-6.

18 R. Verma, R. Belgamwar and V. Polshettiwar, Plasmonic Photocatalysis for CO_2 Conversion to Chemicals and Fuels, *ACS Mater. Lett.*, 2021, **3**(5), 574–598, DOI: 10.1021/acsmaterialslett.1c00081.

19 X. Li, H. O. Everitt and J. Liu, Confirming nonthermal plasmonic effects enhance CO_2 methanation on Rh/TiO_2 catalysts, *Nano Res.*, 2019, **12**(8), 1906–1911, DOI: 10.1007/s12274-019-2457-x.

20 X. Li, X. Zhang, H. O. Everitt and J. Liu, Light-Induced Thermal Gradients in Ruthenium Catalysts Significantly Enhance Ammonia Production, *Nano Lett.*, 2019, **19**(3), 1706–1711, DOI: 10.1021/acs.nanolett.8b04706.

21 X. Zhang, X. Li, M. E. Reish, D. Zhang, N. Q. Su, Y. Gutiérrez, F. Moreno, W. Yang, H. O. Everitt and J. Liu, Plasmon-Enhanced Catalysis: Distinguishing Thermal and Nonthermal Effects, *Nano Lett.*, 2018, **18**(3), 1714–1723, DOI: 10.1021/acs.nanolett.7b04776.

22 G. Baffou, I. Bordacchini, A. Baldi and R. Quidant, Simple experimental procedures to distinguish photothermal from hot-carrier processes in plasmonics, *Light: Sci. Appl.*, 2020, **9**(1), 108, DOI: 10.1038/s41377-020-00345-0.

23 P. K. Jain, Taking the Heat Off of Plasmonic Chemistry, *J. Phys. Chem. C*, 2019, **123**(40), 24347–24351, DOI: 10.1021/acs.jpcc.9b08143.

24 L. Zhou, D. F. Swearer, C. Zhang, H. Robatjazi, H. Zhao, L. Henderson, L. Dong, P. Christopher, E. A. Carter, P. Nordlander, *et al.*, Quantifying hot carrier and thermal

contributions in plasmonic photocatalysis, *Science*, 2018, **362**(6410), 69–72, DOI: 10.1126/science.aat6967.

25 H. Robatjazi, A. Schirato, A. Alabastri, P. Christopher, E. A. Carter, P. Nordlander and N. J. Halas, Reply to: Distinguishing thermal from non-thermal contributions to plasmonic hydrodefluorination, *Nat. Catal.*, 2022, **5**(4), 247–250, DOI: 10.1038/s41929-022-00768-5.

26 Z. Geng, Y. Yu, A. J. Offen and J. Liu, Achieving maximum overall light enhancement in plasmonic catalysis by combining thermal and non-thermal effects, *Nat. Catal.*, 2023, **6**(12), 1241–1247, DOI: 10.1038/s41929-023-01045-9.

27 C. Zhan, B.-W. Liu, Y.-F. Huang, S. Hu, B. Ren, M. Moskovits and Z.-Q. Tian, Disentangling charge carrier from photothermal effects in plasmonic metal nanostructures, *Nat. Commun.*, 2019, **10**(1), 2671, DOI: 10.1038/s41467-019-10771-3.

28 Y. Sivan, J. H. Baraban and Y. Dubi, Experimental practices required to isolate thermal effects in plasmonic photo-catalysis: lessons from recent experiments, *OSA Continuum*, 2020, **3**(3), 483–497, DOI: 10.1364/OSAC.376809.

29 M. L. Brongersma, N. J. Halas and P. Nordlander, Plasmon-induced hot carrier science and technology, *Nat. Nanotechnol.*, 2015, **10**(1), 25–34, DOI: 10.1038/nnano.2014.311.

30 R. C. Elias and S. Linic, Elucidating the Roles of Local and Nonlocal Rate Enhancement Mechanisms in Plasmonic Catalysis, *J. Am. Chem. Soc.*, 2022, **144**(43), 19990–19998, DOI: 10.1021/jacs.2c08561.

31 E. Cortés, R. Grzeschik, S. A. Maier and S. Schlücker, Experimental characterization techniques for plasmon-assisted chemistry, *Nat. Rev. Chem.*, 2022, **6**(4), 259–274, DOI: 10.1038/s41570-022-00368-8.

32 J. Gargiulo, M. Herran, I. L. Violi, A. Sousa-Castillo, L. P. Martinez, S. Ezendam, M. Barella, H. Giesler, R. Grzeschik, S. Schlücker, *et al.*, Impact of bimetallic interface design on heat generation in plasmonic Au/Pd nanostructures studied by single-particle thermometry, *Nat. Commun.*, 2023, **14**(1), 3813, DOI: 10.1038/s41467-023-38982-9.

33 A. J. Offen, Z. Geng, Y. Yu and J. Liu, "A Lot's in a Name": Insights from Debates on Thermal and Nonthermal Effects in Plasmonic Catalysis, *ACS Appl. Energy Mater.*, 2023, **6**(23), 11762–11772, DOI: 10.1021/acsaem.3c01929.

34 L. Mascaretti and A. Naldoni, Hot electron and thermal effects in plasmonic photocatalysis, *J. Appl. Phys.*, 2020, **128**(4), 041101, DOI: 10.1063/5.0013945.

35 R. Verma, G. Sharma and V. Polshettiwar, The paradox of thermal vs. non-thermal effects in plasmonic photocatalysis, *Nat. Commun.*, 2024, **15**(1), 7974, DOI: 10.1038/s41467-024-51916-3.

36 Z. Geng, Y. Yu and J. Liu, Broadband Plasmonic Photocatalysis Enhanced by Photothermal Light Absorbers, *J. Phys. Chem. C*, 2023, **127**(36), 17723–17731, DOI: 10.1021/acs.jpcc.3c03639.

37 X. Li, H. O. Everitt and J. Liu, Synergy between thermal and nonthermal effects in plasmonic photocatalysis, *Nano Res.*, 2020, **13**(5), 1268–1280, DOI: 10.1007/s12274-020-2694-z.

38 O. Henrotte, Š. Kment and A. Naldoni, Mass Transport Limitations in Plasmonic Photocatalysis, *Nano Lett.*, 2024, **24**(29), 8851–8858, DOI: 10.1021/acs.nanolett.4c01386.

39 L. Hurtado, A. Mohan, U. Ulmer, R. Natividad, A. A. Tountas, W. Sun, L. Wang, B. Kim, M. M. Sain and G. A. Ozin, Solar CO2hydrogenation by photocatalytic foams, *Chem. Eng. J.*, 2022, **435**, 134864, DOI: 10.1016/j.cej.2022.134864.

40 A. A. Tountas, A. Dreher, W. Zhou, A. Mohan, N. P. Kherani, G. A. Ozin and M. M. Sain, Light-harvesting properties of photocatalyst supports—no photon left behind, *npj Comput. Mater.*, 2024, **10**(1), 239, DOI: 10.1038/s41524-024-01409-0.

41 J. Y. Y. Loh, A. Mohan, A. G. Flood, G. A. Ozin and N. P. Kherani, Waveguide photoreactor enhances solar fuels photon utilization towards maximal optoelectronic – photocatalytic synergy, *Nat. Commun.*, 2021, **12**(1), 402, DOI: 10.1038/s41467-020-20613-2.

42 F. J. Heiligtag, M. J. I. Airaghi Leccardi, D. Erdem, M. J. Süess and M. Niederberger, Anisotropically structured magnetic aerogel monoliths, *Nanoscale*, 2014, **6**(21), 13213–13221, DOI: 10.1039/C4NR04694C.

43 A. L. Luna, S. Papadopoulos, T. Kyburz, E. Tervoort, L. Novotny and M. Niederberger, Insights into light and mass transport in nanoparticle-based aerogels: the advantages of monolithic 3D photocatalysts, *J. Mater. Chem. A*, 2021, **9**(39), 22380–22391, DOI: 10.1039/D1TA05194F.

44 M. Schreck, N. Kleger, F. Matter, J. Kwon, E. Tervoort, K. Masania, A. R. Studart and M. Niederberger, 3D Printed Scaffolds for Monolithic Aerogel Photocatalysts with Complex Geometries, *Small*, 2021, **17**(50), 2104089, DOI: 10.1002/smll.202104089.

45 F. Rechberger and M. Niederberger, Translucent nanoparticle-based aerogel monoliths as 3-dimensional photocatalysts for the selective photoreduction of CO_2 to methanol in a continuous flow reactor, *Mater. Horiz.*, 2017, **4**(6), 1115–1121, DOI: 10.1039/C7MH00423K.

46 S. Muñoz, A. Navarrete, Á. Martín, R. Dittmeyer and M. J. Cocero, Carbon Dioxide Hydrogenation by Means of Plasmonic Resonance Activation in Silica Aerogel Media, *Materials*, 2018, **11**(11), 2134, DOI: 10.3390/ma11112134.

47 Y. Özbakır, A. Jonáš, A. Kiraz and C. Erkey, An aerogel-based photocatalytic microreactor driven by light guiding for degradation of toxic pollutants, *Chem. Eng. J.*, 2021, **409**, 128108, DOI: 10.1016/j.cej.2020.128108.

48 S. Bhatta, D. Nagassou, S. Mohsenian and J. P. Trelles, Photo-thermochemical decomposition of carbon-dioxide in a direct solar receiver-reactor, *Sol. Energy*, 2019, **178**, 201–214, DOI: 10.1016/j.solener.2018.12.019.

49 Y. Lu, H. Yu, S. Chen, X. Quan and H. Zhao, Integrating Plasmonic Nanoparticles with TiO_2 Photonic Crystal for Enhancement of Visible-Light-Driven Photocatalysis, *Environ. Sci. Technol.*, 2012, **46**(3), 1724–1730, DOI: 10.1021/es202669y.

50 T. Raja Mogan, J. Zhang, L. S. Ng, S. K. Boong, C. Chong, J.-K. Lee, H. Li and H. K. Lee, Harmonizing Plasmonic and Photonic Effects to Boost Photocatalytic H_2 Production over 550 mmol h^{-1} $gcat^{-1}$, *Angew. Chem., Int. Ed.*, 2024, **63**(16),

e202401277, DOI: 10.1002/anie.202401277, acccessed 2025/11/09.

51 B. Hosticka, P. M. Norris, J. S. Brenizer and C. E. Daitch, Gas flow through aerogels, *J. Non-Cryst. Solids*, 1998, **225**, 293–297, DOI: 10.1016/S0022-3093(98)00130-6.

52 Y. K. Mishra, G. Modi, V. Cretu, V. Postica, O. Lupan, T. Reimer, I. Paulowicz, V. Hrkac, W. Benecke, L. Kienle, *et al.*, Direct Growth of Freestanding ZnO Tetrapod Networks for Multifunctional Applications in Photocatalysis, UV Photodetection, and Gas Sensing, *ACS Appl. Mater. Interfaces*, 2015, **7**(26), 14303–14316, DOI: 10.1021/acsami.5b02816.

53 Y. K. Mishra, S. Kaps, A. Schuchardt, I. Paulowicz, X. Jin, D. Gedamu, S. Freitag, M. Claus, S. Wille, A. Kovalev, *et al.*, Ceramics: Fabrication of Macroscopically Flexible and Highly Porous 3D Semiconductor Networks from Interpenetrating Nanostructures by a Simple Flame Transport Approach, *Part. Part. Syst. Charact.*, 2013, **30**(9), 731–731, DOI: 10.1002/ppsc.201370034, acccessed 2025/04/16.

54 F. Schütt, M. Zapf, S. Signetti, J. Strobel, H. Krüger, R. Röder, J. Carstensen, N. Wolff, J. Marx, T. Carey, *et al.*, Conversionless efficient and broadband laser light diffusers for high brightness illumination applications, *Nat. Commun.*, 2020, **11**(1), 1437, DOI: 10.1038/s41467-020-14875-z.

55 L. M. Saure, N. Kohlmann, H. Qiu, S. Shetty, A. Shaygan Nia, N. Ravishankar, X. Feng, A. Szameit, L. Kienle, R. Adelung, *et al.*, Hybrid Aeromaterials for Enhanced and Rapid Volumetric Photothermal Response, *ACS Nano*, 2023, **17**(22), 22444–22455, DOI: 10.1021/acsnano.3c05329.

56 J. Lumma, T. Tjardts, E. Greve, L. M. Saure, S. Veziroglu, R. Adelung, L. Kienle, N. Wolff and F. Schütt, Synthesis of Highly Porous 3D Cerium Oxide Networks Designed for Catalytic Applications, *Cryst. Growth Des.*, 2024, **24**(12), 4914–4923, DOI: 10.1021/acs.cgd.3c01197.

57 X. Zhang, P. Li, Á. Barreda, Y. Gutiérrez, F. González, F. Moreno, H. O. Everitt and J. Liu, Size-tunable rhodium nanostructures for wavelength-tunable ultraviolet plasmonics, *Nanoscale Horiz.*, 2016, **1**(1), 75–80, DOI: 10.1039/C5NH00062A.

58 L. W. Hrubesh and R. W. Pekala, Thermal properties of organic and inorganic aerogels, *J. Mater. Res.*, 1994, **9**(3), 731–738, DOI: 10.1557/JMR.1994.0731.

59 B. Shi, L. Xie, B. Ma, Z. Zhou, B. Xu and L. Qu, Preparation and Properties of Highly Transparent SiO_2 Aerogels for Thermal Insulation, *Gels*, 2022, **8**(11), 744, DOI: 10.3390/gels8110744.

60 H.-P. Ebert, Thermal Properties of Aerogels, in *Aerogels Handbook*, ed. M. A. Aegerter, N. Leventis and M. M. Koebel, Springer, New York, 2011, pp. 537–564.

61 Y. Sivan, J. Baraban, I. W. Un and Y. Dubi, Comment on "Quantifying hot carrier and thermal contributions in plasmonic photocatalysis", *Science*, 2019, **364**(6439), eaaw9367, DOI: 10.1126/science.aaw9367.

62 A. Emmerling, R. Petricevic, A. Beck, P. Wang, H. Scheller and J. Fricke, Relationship between optical transparency and nanostructural features of silica aerogels, *J. Non-Cryst. Solids*, 1995, **185**(3), 240–248, DOI: 10.1016/0022-3093(95)00021-6.

63 X. Ji, Y. Du and X. Zhang, Elaborate Size-Tuning of Silica Aerogel Building Blocks Enables Laser-Driven Lighting, *Adv. Mater.*, 2022, **34**(6), 2107168, DOI: 10.1002/adma.202107168.

64 P. Dieudonne and J. Phalippou, Textural Properties of Densified Aerogels, *J. Sol-Gel Sci. Technol.*, 1999, **14**(3), 249–256, DOI: 10.1023/A:1008765428511.

65 W. He, X. Huang, X. Ma and J. Zhang, Significant temperature effect on the LSPR properties of noble metal nanoparticles, *J. Opt.*, 2022, **51**(1), 142–153, DOI: 10.1007/s12596-021-00766-z.

66 W. Stöber, A. Fink and E. Bohn, Controlled growth of monodisperse silica spheres in the micron size range, *J. Colloid Interface Sci.*, 1968, **26**(1), 62–69, DOI: 10.1016/0021-9797(68)90272-5.

67 Silica Aerogel, https://www.aerogel.org/?p=1406 (accessed 2023).

68 D. Bokov, A. Turki Jalil, S. Chupradit, W. Suksatan, M. Javed Ansari, I. H. Shewael, G. H. Valiev and E. Kianfar, Nanomaterial by Sol-Gel Method: Synthesis and Application, *Adv. Mater. Sci. Eng.*, 2021, **2021**(1), 5102014, DOI: 10.1155/2021/5102014.

69 R. S. Fernandes, I. M. Raimundo and M. F. Pimentel, Revising the synthesis of Stöber silica nanoparticles: A multivariate assessment study on the effects of reaction parameters on the particle size, *Colloids Surf., A*, 2019, **577**, 1–7, DOI: 10.1016/j.colsurfa.2019.05.053.